On the impact of dropsondes on the EC IFS model (Cy47r1) analysis of convection during OTREC

Stipo Sentić[1], Peter Bechtold[2], Željka Fuchs-Stone[1,3], Mark Rodwell[2], and David J. Raymond[1,3]

[1]Climate and Water Consortium, New Mexico Tech, Socorro, NM, USA
[2]European Center for Medium Range Weather Forecast, Reading, UK
[3]Physics Department, New Mexico Tech, Socorro, NM, USA

Correspondence: Stipo Sentić (stipo.sentic@nmt.edu)

Abstract. The Organization of Tropical East Pacific Convection (OTREC) field campaign, conducted August through October 2019, focuses on studying convection in the East Pacific and the Caribbean. An unprecedented number of dropsondes were deployed (648) during 22 missions to study the region of strong sea surface temperature (SST) gradients in the East Pacific region, the region just off the coast of Columbia, and in the uniform SST region in the southwest Caribbean. The dropsondes were assimilated in the European Center for Medium Range Weather Forecast model. This study quantifies departures, observed minus the model value of a variable, in dropsonde denial experiments, and studies time series of convective variables: saturation fraction which measures moisture, and instability index and deep convective inhibition which quantify atmospheric stability and boundary layer stability to convection, respectively. Departures are small whether dropsondes are assimilated or not, except in a special case of a precursor to tropical storm Ivo where wind departures are significantly larger when dropsondes are not assimilated. Departures are larger in cloudy regions compared to cloud free regions when comparing a vertically integrated departure with a cloudiness estimation. Above mentioned variables are all well represented by the model when compared to observations, with some systematic deviations in and above the boundary layer. Time series of these variables show artificial convective activity in the model, in the East Pacific region off the coast of Costa Rica, which we hypothesize occurs due to overestimation of moisture content in that region.

1 Introduction

The Organization of Tropical East Pacific Convection (OTREC) field campaign was performed from Aug 5 to Oct 3, 2019, in the regions of far East Pacific and the Caribbean. The main goal of the OTREC field campaign Fuchs-Stone et al. (2020); Raymond and Fuchs-Stone (2021) is to study the convection in the East Pacific. The location of dropsonde deployment during OTREC is shown in Figure 1: the East Pacific boxes; B2, B3, and B1a (B1a off the coast of Colombia), and a box in the Caribbean, B1b. Fuchs-Stone et al. (2020) presented preliminary results of the OTREC field campaign. They found that active convection in the region exhibits bottom heavy mass flux profiles, with more top heavy mass flux at the north of the B2 box. Raymond and Fuchs-Stone (2021), using OTREC data, identified three parameters important for convection in the region: saturation fraction, instability index, and deep convective inhibition (DCIN). These parameters were found also in previous research to be important in characterizing convection.

25 The East Pacific area of the tropics is well known for tropical cyclone genesis (e.g. Zehnder, 1991; Zehnder et al., 1999; Molinari and Vollaro, 2000), whether from initiation from local conditions, or from African easterly waves which travel through the region. Another goal of the OTREC field campaign was to collect field data for study of the interaction of passing African easterly waves and local convection, and its influence on tropical cyclone genesis, and to investigate if any easterly waves originated in the area of the OTREC field campaign. Since field data is sparse in the region, researchers often use reanalysis

30 to study these interactions, so an overarching goal is to gauge the performance of operational models and reanalysis in this area. Often utilised in study of these phenomena are the European Center for Medium-Range Weather Forecasts (ECMWF) operational analysis and reanalysis (e.g. Hersbach et al., 2020).

A number of previous studies looked at the influence of dropsondes and radiosondes on the ECMWF analysis and reanalysis in other regions of the planet. For example, in the African Monsoon Multidisciplinary Analysis (AMMA) project Agustí-

35 Panareda et al. (2010) found that an extended radiosonde network influenced the analysis temperature and moisture in the boundary layer, thus affecting the model cloudiness and convection. They also found that African easterly waves could be affected by the analysis departures from observations. Harnisch and Weissmann (2010) found that assimilating dropsondes in regions near the cores of tropical cyclones had a positive impact on the analysis and track forecasts, during The Observing System Research and Predictability Experiment (THORPEX) Pacific Asian Regional Campaign (T-PARC) 2008. Schindler et al.

40 (2020) found, during the North Atlantic Waveguide and Downstream Impact Experiment (NAWDEX), that additional dropsondes conservatively yet positively influence the forecast error of the ECMWF data. Chan et al. (2018) found that assimilating data for a tropical cyclone decreases the forecast errors by 13%, and produces a better intensity and track forecasts. They found that assimilated humidity largely contributed to these improvements. In other models, for example, Feng and Wang (2019) studied the influence of dropsondes on modeling rapid intensification of hurricane Patricia (2015). Including dropsondes im-

45 proves accuracy of outflow and thermodynamic analysis, and improves rapid intensification forecast. These and other ECMWF studies (e.g. Keil and Cardinali, 2004; Tompkins et al., 2005; Harnisch et al., 2011) have been performed outside the east Pacific region. As studies of African easterly waves rely heavily on reanalysis data Molinari and Vollaro (2000); Hodges et al. (2003); Kiladis et al. (2006); Chen (2006); Mekonnen et al. (2006); Ruti and Dell'Aquila (2010); Serra et al. (2010); Janiga and Thorncroft (2013); Rydbeck and Maloney (2015), it is imperative to understand the influence of lack of free tropospheric

50 data on these analyses.

The OTREC field campaign is the first field campaign since EPIC2001 Petersen et al. (e.g. 2003); Raymond et al. (e.g. 2004) that focused on this region with an unprecedented amount of tropospheric data collected. One of the main instruments used during the OTREC field campaign were NRD41 dropsondes Vömel et al. (2021) launched from the UCAR/NCAR Gulfstream-V aircraft, in addition to radiosonde launches from three land based sites: Limon and Santa Cruz on the east and west coasts

55 of Costa Rica, respectively, and Nuqui on the Pacific coast of Colombia. 648 dropsondes were successfully deployed during OTREC. The configuration of the drops during OTREC, i.e. high resolution dropsondes deployed from 13 km (EPIC2001 had sonde data up to 6.3 km) spaced about 1 degree horizontally, allow for a more accurate assessment of fields sensitive to the horizontal data distribution, like vorticity and divergence, and other derived fields.

The European Center (EC) assimilated the dropsonde data in their operational analysis and reanalysis. This paper quan-

60   titatively assesses the impact of high resolution dropsonde data on the EC analysis and tropical convection during OTREC. We perform an experiment with the EC operational model assimilating dropsondes (labeled YDPS throughout the paper), and experiment with no dropsondes assimilated (labeled NDPS throughout the paper), and we compare these two experiments to observations (dropsondes). Note that radiosondes are always assimilated. Time series of reanalysis thermodynamic variables are also assessed.

65   Section 2 describes the data and variables used in this study. We look at basic fields in the model (zonal and meridional wind, moisture and temperature) on specified levels for both experiments, and compare them to observed values from the dropsondes, in section 3. We also estimate vorticity since the mid level values of vorticity are often used to diagnose the passage of easterly waves. In section 4 we look at the influence of cloudiness on the dropsonde assimilation, and compare the modeled and observed saturation fraction, instability index, and DCIN. Finally, section 5 assesses the EC operational model

70   (since it assimilated the dropsondes) and time series of thermodynamic variables obtained from it to measure the performance of the model for convective and non-convective regions.

2   Data and methods

This study exclusively uses OTREC dropsonde in situ observations UCAR/NCAR Earth Observing Laboratory (2019); Fuchs-Stone et al. (2020); Raymond and Fuchs-Stone (2021); Vömel et al. (2021) while a 3D variational analysis produced using those

75   dropsondes serves as a 3D proxy of the observations. The 3D-var analysis is calculated by a penalty function minimization Raymond and López Carrillo (2011); López Carrillo and Raymond (2011) which produces a gridded data set where the inter-polated values in between dropsondes satisfy the mass continuity equation. This 3D-var approach was used in many previous studies of convection Gjorgjievska and Raymond (2014); Fuchs-Stone et al. (2020); Raymond and Fuchs-Stone (2021).

Model data used is the European Center operational model (IFS, version Cy47r1) run from Aug 7 to Sep 30, 2019, in

80   a dropsonde assimilated mode (labeled YDPS throughout this paper), and dropsondes *not* assimilated mode (labeled NDPS throughout this paper). The departures of the model state from the observations are denoted by:

$$x = x_{observation} - x_{model}, \tag{1}$$

where x is one of the basic fields: zonal wind u, meridional wind v, water vapor mixing ratio q, and temperature T. Note that positive values of departure denote deficit in the model. The departures are computed collocating the model data in space and time to the observation location. Therefore, the results are for the reported significant levels (i.e. where the observation value

85   changes significantly), but we show departures for mandatory levels up to the 200 hPa pressure level. Vorticity and divergence, and their departures, are estimated by using the observed and model values of zonal and meridional winds. Although the point data we get from the above procedure is produced in a 4D variational procedure, we assume the drops were done simultaneously for the vorticity estimation. Since there is lag between dropsonde drop times, this only gives estimates of vorticity departures and not real vorticity departures, although the OTREC flights were designed to minimize problems with

90   time skew in calculating vorticity, divergence, and other derived fields.

Furthermore, we use thermodynamic variables shown in previous research Fuchs-Stone et al. (2020); Raymond and Fuchs-Stone (2021) to be significant in diagnosing the development of convection: saturation fraction, instability, and DCIN. Saturation fraction is defined as precipitable water divided by saturated precipitable water, which is a measure of column relative humidity. Instability index, defined as saturated moist entropy between 1 and 3 km minus the saturated moist entropy from 5 to 7 km, is a measure of the mid to low tropospheric moist convective stability. Contrary to intuition, the lower the instability index, the more conducive the environment is to deep convection. This was found in many studies of convection, both isolated convection Raymond and Sessions (2007); Sessions et al. (2015); Sentić and Sessions (2017) and organized convection like hurricanes and the Madden-Julian Oscillation Gjorgjievska and Raymond (2014); Raymond et al. (2014); Sentić et al. (2015). Deep Convective Inhibition (DCIN), defined as the mean saturated moist entropy from 1.5 to 2 km minus the mean moist entropy from 0 to 1 km in the boundary layer, was also shown to play a significant role in convective development Sentić et al. (2015); Fuchs-Stone et al. (2020); Raymond and Fuchs-Stone (2021). Convection develops when DCIN is small or negative.

European Center operational data is used for calculating the diurnal cycle of the above variables for non-convective, and convective 1 by 1 degree cells. We define non-convective and convective cells as having moisture convergence less than 0.5 kW m^{-2} and greater than 2 kW m^{-2}, respectively, where moisture convergence is defined as:

$$\Delta_m = -\int\limits_{p_s}^{p_t} \nabla \cdot (q\mathbf{v})dp, \tag{2}$$

where p_s and p_t are surface and top pressure, respectively, q is the mixing ratio, and $\mathbf{v}$ is the horizontal wind vector. For selected cells the diurnal cycle is calculated to produce a mean diurnal cycle for both non-convective and convective cells.

Also used are NOAA GOES-R 16 channel 14 infrared temperature, averaged in a 0.5 by 0.5 degree box around each dropsonde, to quantify cloudiness Schmit et al. (2017), and ERA5 ECMWF data Hersbach et al. (2020).

3 Model analysis

This section examines the departures of EC zonal and meridional winds, water vapor mixing ratio, and potential temperature from actual dropsonde values, for the two experiments with and without dropsondes included in the EC analysis (YDPS and NDPS). First, horizontal departures are examined as a function of longitude and latitude (section 3.0.1) for a select pressure level. Next, vertical profiles of departures are shown as a function of pressure (section 3.1). Understanding the locations of the largest departures can inform us about systematic model errors and random errors in the placement of convective systems. A special case is also examined; a single OTREC research flight done in tandem with the NOAA P3 mission into the precursor of tropical storm Ivo. Finally, we examine estimates of vorticity and divergence for convective regions in section 3.2.

3.0.1 Horizontal distribution of background departures

The lower troposphere above the boundary-layer is critical for the development of convection. We found the largest departures (defined in equation 1) at the 700 hPa level. Figure 2 displays the mean departures for zonal and meridional winds, while

120 the departures for specific humidity and temperature are displayed in Figure 3. The top row of panels shows mean dropsonde observations, middle row departures of the YDPS experiment, and bottom row departures of the NDPS experiment for zonal wind on the left and meridional on the right, for Figure 2. Both zonal and meridional wind have smaller departures in the YDPS experiment than in the NDPS experiment for all boxes. In the region northwest of the B2 box, however, the departures are large in the NDPS experiment. There was only one flight in the north west region, in box B3. This special case was

125 flown on Aug 18, when the NCAR Gulfstream-V flew in conjunction with the NOAA P3 operational aircraft to investigate the precursor to tropical storm Ivo. Departures in box B3 are statistically significant which is obvious when mean departures are plotted for each individual flight (not shown)—the mean departures in box B3 are larger than the mean departures for each other individual flight. Lack of dropsondes in this region in the model might have negatively impacted prediction of disturbances which developed into tropical storm Ivo. This suggests that the model might need more data in the pre-storm

130 phase of a developing tropical cyclone to ingest and produce better initial conditions, at least in the East Pacific tropical region. The regions of boxes B2, B1a and B1b seem less sensitive to absence of dropsondes in the denial experiments since they do not show drastic changes in departures between the YDPS and NDPS experiments.

Figure 3 shows a similar picture. For both water vapor mixing ratio and temperature, the NDPS experiment shows larger values of departures compared to the YDPS experiment. However, in the B3 box we do not see larger than average departures

135 in thermodynamic values; only the zonal and meridional winds suffered large departures in B3 box mentioned above. This suggests that assimilation of wind fields from satellite data and other sources could be refined in organised convection conditions as exhibited in the case of precursor to tropical storm Ivo.

3.1 Vertical structure of departures

Figure 4 shows the mean and standard deviation of departures from the observations, for zonal wind (figure 4a), meridional

140 wind (figure 4b), mixing ratio (figure 4c), and potential temperature (figure 4d), for both the YDPS (black lines) and the NDPS experiment (red lines). The zonal and meridional wind both show smaller departures and standard deviations in the YDPS run, with the NDPS experiment having a small negative bias (see equation 1) in the layer from about 800 to 500 hPa for the zonal wind, and the meridional wind having a positive bias in the layer from about 900 to 600 hPa. These departures are not large considering, for example, that the relative error is about 25% and 40% for the YDPS and NDPS experiment zonal wind

145 mean of about 2 m s^{-1} at about 700 hPa, respectively (not shown). The mixing ratio (figure 4c) shows a slight dry model bias throughout the troposphere with a relative error less than 4% to 6 % between the observations and the YDPS and NDPS experiments, respectively (not shown). Similarly for potential temperature, there is a slight cold model bias in the model for both the YDPS and NDPS experiment. In all cases, the inclusion of the soundings contributed to decreased spread of the departures as seen in the smaller range of the standard deviation. Both in the zonal and horizontal wind, largest departures

150 occur around 700 hPa in the YDPS and NDPS experiments.

The departures above were computed by averaging over all the research flights. Here we focus on the special case in box B3, addressed in section 3.0.1. The horizontal averages in Figures 2 and 3 show the B3 box where we find largest departures in zonal and meridional wind. Figure 5 shows the averages similar to Figure 4 but only for the research flight in box B3. The

zonal wind, meridional wind, and temperature, show large departures in the NDPS experiment, and including the dropsondes
155 drastically reduces the mean departures and the standard deviation of the departures in the YDPS experiment. In pre-tropical
storm conditions the model might have issues in assimilating data as in the case of the precursor to tropical storm Ivo. This
case is complicated with the presence of local gap winds like the Tehuantepec jet, effects of which we leave to future studies.

In summary, departures are small on average as the observing system is well constrained and determined by infrared and
microwave satellite observations, and conventional observations, especially over sea as over land satellite channels with strong
160 sensitivities close to the surface cannot be assimilated Geer et al. (2017, 2018, 2019). However, in strongly perturbed synoptical
conditions as in tropical cyclone environments departures can be large. The next section derives estimates of vorticity and
divergence from the dropsonde data to understand how the departures in the basic wind fields affects the departures in these
derived fields.

3.2 Vorticity and divergence estimates

165 Relative vorticity and divergence are important for study of convection and identifying the passage of easterly waves. Therefore,
it is necessary to estimate these variables and gauge how assimilating dropsonde data contributes to the integrity of the analysis.

Since we do not have blacklisted profiles of the EC model relative vorticity and divergence as we do for the basic fields
from the previous sections (wind, mixing ratio, and potential temperature), we estimate these fields from the dropsonde denial
experiments by first gridding the point data onto a regular grid. The vorticity and divergence are then calculated using finite
170 differences, and the calculation is confirmed by comparing the circulation around the perimeter of interest calculated using the
vorticity and the circulation theorem:

$$\Gamma = \oint_{\delta S} \boldsymbol{v} \cdot d\boldsymbol{l} = \int \int_S \zeta dS \tag{3}$$

where Γ is the circulation, $\boldsymbol{v}$ is the wind speed, S is the area over which circulation is being calculated over, and ζ is the
vocticity. The circulations computed from both methods agree to within 10% in the lowest 500 hPa giving us confidence in
the derived vorticity and divergence. However, larger errors appear above 500 hPa, hence those levels are excluded from the
175 following vorticity analysis. During an OTREC research flight the dropsondes were dropped over a span of 6 hours, but for
the purpose of estimating the vorticity and divergence we assume that the dropsondes have been dropped at the same time.
However, the OTREC flight patterns have been designed to minimize the time skew in calculating vorticity and divergence.
For consistency with previous research (Fuchs-Stone et al., 2020), the divergence and vorticity are averaged in the regions of
developing and decaying convection as tabulated in Table 1 from Fuchs-Stone et al. (2020).

180 Figure 6 shows the vorticity and divergence departures calculated for the YDPS and the NDPS experiments, Figure 6a
and 6b for all the cases from Fuchs-Stone et al. (2020), and Figure 6c and 6d, for the special case in the B3 box. The B3
box case (figure 6c and 6d) does not show a standard deviation line because it is a single average over the west half of the
B3 box. Both the YDPS and NDPS experiments in Figure 6a and 6b produce reasonably small mean vorticity departures,
but assimilation of dropsondes improves the standard deviation of departures. Assimilation of dropsondes also benefits the
185 divergence calculation in the lower troposphere where there is also a reduction of the standard deviation of the departures

and even the mean of departures. In this estimate, the divergence departures increase both in the mean and the standard deviation for levels higher than 700 hPa even for the YDPS experiment. Since the absolute values of vorticity and divergence are between 0 and 0.02 ks^{-1} (not shown), the departures are relatively small (10-45% below 700 hPa). However, there seems to be a systematic underestimation of the divergence below 700 hPa for both the YDPS and the NDPS experiments. The B3

190 box case (figure 6c and 6d) shows large differences in the vorticity departures between the YDPS and NDPS experiments. Assimilating dropsondes (YDPS experiment) decreases the departure value for the layer between 500 and 900 hPa, however both experiments show larger departures below 900 hPa. The divergence shows similar departures for both experiments for the B3 box.

In summary, we find that there is a small difference between the estimated vorticity and divergence for the YDPS and the

195 NDPS experiments, with a systematically larger departure of divergence for both experiments. We also find that for the special case, B3, departures of vorticity are much smaller when dropsondes are assimilated.

4 Cloudiness effects and thermodynamic variables

This section examines the influence of cloudiness on the assimilation of dropsondes during OTREC. Also, we look at derived fields found useful in studying convection, defined in section 2; saturation fraction, instability index, and DCIN.

200 The OTREC field campaign sampled the tropospheric environment in both convective, cloudy, and non-convective, cloud-free, conditions. Therefore, it is possible to assess the influence of dropsonde assimilation in the EC model for cloudy and cloud free regions. For each dropsonde spot we calculate a measure of the tropospheric departure at the location by vertically integrating each variable departure:

$$x^* = \frac{1}{p_s - p_t} \int_{p_s}^{p_t} |x| dp \qquad (4)$$

where x is the departure (defined in equation 1) for any of the basic variables of interest (u, v, T, and q), p is pressure, and p_t

205 and p_s are the top and surface pressure, respectively. For each dropsonde spot a corresponding infrared temperature is averaged as a measure of cloudiness, cloud free regions defined by large values of infrared temperature, and cloudy regions defined with lower IR temperatures. The vertical departures and the cloudiness proxy are then compared. As an example, Figure 7 shows u^* for two soundings. A smaller vertically integrated departure is shown for the first dropsonde, Figure 7a, compared to almost a double value for a previous sounding. In these examples there is a difference in the vertical distribution of the departure of u

210 but that is not captured in the single number u^*. Determinations of the influence of vertical distribution of departures is left to future work. We compare the vertically integrated departure with infrared temperature over each dropsonde position. We use a 0.5 deg by 0.5 deg box to average the infrared temperature as a measure of cloudiness; we found that the results are not very sensitive to the size of this box.

Figure 8 shows the vertically integrated departures for u, v, q, and T, for the YDPS experiment in black, and the NDPS

215 experiment in red. A linear fit is applied to each scatter for each variable. First, for high values of infrared temperature, e.g. greater than 280 K (fair weather), there is a clustering of points for each variable, with relatively small x^*, which means that

Geoscientific
Model Development
Discussions

in fair weather the EC model has small departures for all variables. Second, for cloudier conditions, i.e. infrared temperature less than 280 K, there is significantly more scatter in all variables, especially in u and v, as indicated by the slope of the fitted lines. The slope of the lines fitted in the wind scatter plots are large than for the mixing ratio and the temperature. q^* and T^*

220 seem to perform well for both cloudy and cloud free conditions. Apart from the line slope, we can infer the performance of assimilating the dropsondes in the model by observing the fit offset. The offset is larger for all the variables for the NDPS experiment, especially for u^* and v^*. These results indicate that dropsonde assimilation has a small improvement on the model performance in both cloudy and cloud free conditions in the OTREC field campaign. Considering that the model assimilates data from many data sources, it is not clear from which data source do these discrepancies arise at this time. Future investigation

225 might reveal which data sources might need improvement in assimilating winds.

Figure 9 shows the scatter plots of saturation fraction (panels a and b), instability index (panels c and d), and DCIN (panels e and f), calculated from the dropsondes (OBS) and the YDPS experiment, on the left, and scatter plots between the YDPS and NDPS experiments on the right. There is excellent agreement between the OBS and YDPS experiment with little scatter, and there is little discrepancy between the experiment with and without dropsondes. This might not be surprising considering the

230 previous section. The moisture and temperature fields are not very sensitive to the assimilated dropsondes as much as the wind field is. DCIN seems to deviate from observations, the YDPS and NDPS experiments both give stronger DCIN compared to OBS. In summary, the variables we find useful in modeling and understanding convection, i.e. saturation fraction, instability index, and somewhat DCIN, seem to be well represented by the EC model in all conditions, this gives confidence in using these fields in reanalysis data.

5   Diurnal variability for convective and non-convective regions

235

Next the time series of thermodynamic variables mentioned in the previous section are examined. We use the 3D-var analysis explained in section 2, and ERA5 analysis data on the days of the flights. The 3D-var analysis of the observational dropsonde data is used to calculate moisture convergence which is used to define convective (moisture convergence greater than 2 kW m^{-2}) and non-convective (moisture convergence less than 0.5 kW m^{-2}) regions in the flight domain. For each of those cases

240 the diurnal cycle of variables is taken at the location of the convective or non-convective one by one degree boxes, and averaged to obtain a mean diurnal cycle of variables for convective and non-convective regions. Figure 10 shows the mean diurnal cycle of EC model moisture convergence, infrared temperature (from observations), saturation fraction, instability index, and DCIN, for convective (red) and non-convective regions (black). Plotted are convective regions total mean diurnal cycle (red), which is decomposed into boxes B2 (blue) and B1a (green) for the reasons mentioned below. The diurnal cycles are calculated from

245 1047 individual cases for the non-convective case, 99 for the convective case, 33 for the B1a case, and 66 for the B2 case. The 6 B1b convective cases are excluded because the mean calculated from these is not statistically significant for such a low case count. Vertical thin black lines bracket the period when the Gulfstream-V flew.

There is a stark difference between the mean diurnal cycle of convective regions (red line) and non-convective regions (black line). Convective regions show much lower values of instability index and DCIN, and at the same time show larger

250 values of saturation fraction, compared to non-convective regions. In convective regions, the diurnal changes of saturation fraction, instability index, and DCIN, agree with previous research, namely that instability index and DCIN decrease between 0 and 12 UTC, and that saturation fraction increases. The increase of saturation fraction is in agreement with increase of moisture convergence, peaking around 12 UTC (moisture convergence is associated with convection as is saturation fraction). The infrared temperature also shows stark contrast between the convective and non-convective regions. Non-convective regions

255 show a steady high value of infrared temperature characteristic of convection free regions, while the convective regions show a characteristic lag in the infrared temperature minimum compared to the 12 UTC moisture convergence maximum (Bechtold et al., 2014), associated with stratiform convection which follows deep convection. We notice another maximum in moisture convergence around 19 UTC for convective regions (red line). Flight notes and comparisons of satellite imagery and moisture convergence of the ERA5 data show that this secondary maximum is artificial.

260 Decomposing the convective regions into convective regions in box B2 (blue line), and box B1a (green line), shows that the secondary maximum is a consequence of the model performance in box B2. Convective regions in box B1a agree with our observations, even showing that the convection in B1a starts earlier in the day (as early as 8 UTC). Box B2, on the other hand, shows an exaggerated maximum at about 19 UTC, not seen in observations, and doesn't show up in the diurnal cycle of infrared temperature as a decrease in infrared temperature as expected from deep convection developing into stratiform convection. We

265 speculate that this secondary maximum might come from overestimating the afternoon saturation fraction and underestimating the instability index by the ECMWF model (blue line, after 15 UTC), in the south part of the B2 box. This is a subject of future research.

In summary, while the saturation fraction, instability index, and DCIN, follow the moisture quasi equilibrium which finds its fingerprints in moisture convergence and infrared temperature, we find an artificial convective maximum in box B2 associated

270 with potentially overestimated saturation fraction and underestimated instability index supporting this.

6 Summary and conclusions

This paper evaluates the performance of the ECMWF model during the OTREC field campaign, held during Aug 5 to Oct 3, 2019, in the East Pacific and the Caribbean. The UCAR research aircraft Gulfstream-V performed 22 flights in alternate boxes, dropping a total of 648 successful drops. The retrieved fields: zonal and meridional winds, water vapor mixing ratio, and

275 temperature, versus pressure, were assimilated in the operational EC model. To evaluate the model's performance, in addition to using operational data, two experiments are used: with (YDPS) and without (NDPS) dropsondes assimilated. Departures, defined as model values subtracted from observation values, are calculated at the moment of the drop to quantify the deviation of the model from observations for each dropsonde individually.

The vertical departures' mean and standard deviation have small improvements in all fields by inclusion of the dropsondes

280 in the YDPS experiment. The maximum departures in the NDPS experiment occur around 700 hPa, and investigation of the horizontal departure maps shows that the special case of research flight 6 (Aug 18, 2019), a flight into the precursor of tropical storm Ivo, shows the largest departures both horizontally and vertically. Horizontal maps of all variable departures at 700 hPa

(and other levels, not shown) benefit from assimilating dropsondes by smaller departures. The zonal and meridional winds seem to benefit the most from assimilating dropsondes, by both vertically and horizontally diminished departures, while temperature

285   and mixing ratio have small departures in the NDPS experiment. As a consequence, thermodynamic fields used in previous studies, saturation fraction, instability index, and, to a lesser degree, DCIN, all show good agreement between the observed and model values. Including dropsondes reduces the spread of the scatter between the observed and modeled values of these fields. DCIN seems to be overestimated for large absolute values indicating possible boundary layer departures from observations. There is a small difference between the estimated relative vorticity and divergence for the YDPS and the NDPS experiments,

290   with a systematically larger departure of divergence for both experiments. For the special case, box B3, vorticity departures are reduced when dropsondes are assimilated.

   Vertically integrated departures for dropsonde denial experiments show that there is little departure from observations in cloud free regions. In cloudy regions, these vertical departures show more scatter, i.e. larger departures from observations, especially in the zonal and meridional winds. Moisture shows marginal vertical departure improvement with included dropson-

295   des, while temperature and the winds show a bigger improvement especially for large outlier vertical departures. This suggests that there is room for improvement of satellite derived assimilated winds in cloudy regions.

   We performed an analysis of composites of the diurnal cycle for convective and non-convective regions. Instability index and DCIN decrease, and saturation fraction increases, as expected from previous research, before the onset of convection around 13 UTC. This is consistent with observed decrease of infrared temperature after 13 UTC associated with stratiform convection

300   of the convective life cycle. A secondary maximum in the EC model moisture convergence, which is associated with deep convection, suggests a second episode of convection around 19 UTC. Satellite observations and our fields notes suggest that this secondary maximum is artificial; further decomposition of the convective diurnal cycle into the East pacific and Colombian box shows that this secondary maximum occurs in the East Pacific box. Large saturation fraction during that period in the south of the B2 box in the EC operational data might contribute to the artificial convection developed around 19 UTC.

305   In conclusion, while the EC model performed well in the OTREC campaign there is room for improvement for the assimilated winds, and, to a lesser degree, temperature fields. Further EC model study could reveal the sources of anomalous convection in late afternoon, and improvements could be made to the assimilated wind in cloudy regions. Consequently, further study of the EC model in this region could reveal to what degree we can trust analysis and reanalysis data in the East Pacific region.

310   *Code and data availability.* Code and model departure data used in this study can be found at doi:10.5281/zenodo.5576132. EC model data in figure 10 is proprietary and the reader is directed to the European Center to obtain the operational data used in this study. GOES 16 data was obtained at https://console.cloud.google.com/storage/browser/gcp-public-data-goes-16.

Author contributions. Stipo Sentic analysed the data, plotted the figures, and was the main writer of this manuscript. Peter Bechtold performed the EC model denial experiments and participated in the discussion of the results, while Željka Fuchs-Stone participated in data
315 analysis and discussion of the results. Mark Rodwell produced the blacklist files for the NODPS experiment departure calculation, and David J. Raymond participated in the discussion of the results.

Competing interests. There are no competing interests present.

Geoscientific
Model Development
Discussions

References

Agustí-Panareda, A., Beljaars, A., Cardinali, C., Genkova, I., and Thorncroft, C.: Impacts of Assimilating AMMA Soundings on ECMWF Analyses and Forecasts, Weather and Forecasting, 25, 1142–1160, 2010.

Chan, P., Wu, N., Zhang, C., Deng, W., and Hon, K.: The first complete dropsonde observation of a tropical cyclone over the South China Sea by the Hong Kong Observatory, Weather, 73, 227–234, https://doi.org/10.1002/wea.3095, 2018.

Chen, T.: Characteristics of African Easterly Waves Depicted by ECMWF Reanalyses for 1991–2000, Monthly Weather Review, 134, 3539–3566, 2006.

Feng, J. and Wang, X.: Impact of Assimilating Upper-Level Dropsonde Observations Collected during the TCI Field Campaign on the Prediction of Intensity and Structure of Hurricane Patricia 2015, Mon. Wea. Rev., 147, 3069–3089, https://doi.org/10.1175/MWR-D-18-0305.1, 2019.

Fuchs-Stone, Ž., Raymond, D. J., and Sentić, S.: OTREC2019: Convection Over the East Pacific and Southwest Caribbean, Geophysical Research Letters, 47, e2020GL087 564, 2020.

Geer, A. J., Baordo, F., Bormann, N., Chambon, P., English, S., Kazumori, M., Lawrence, M., Lean, P., Lonitz, K., and Lupu, K.: The growing impact of satellite observations sensitive to humidity, cloud and precipitation, Q.J.R. Meteorol. Soc., 143, 3189–3206, https://doi.org/10.1002/qj.3172, 2017.

Geer, A. J., Lonitz, K., Weston, P., Kazumori, M., Okamoto, K., Zhu, Y., Liu, E., Collard, A., Bell, W., Migliorini, S., Chambon, P., Fourri, N., Kim, M.-J., K opken-Watts, C., and Schraff, C.: All-sky satellite data assimilation at operational weather forecasting centres, Q. J. R. Meteorol. Soc., 144, 1191–1217, https://doi.org/10.1002/qj.3202, 2018.

Geer, A. J., Matricardi, M., and Migliorini, S.: All-sky assimilation of infrared radiances sensitive to mid- and upper-tropospheric moisture and cloud, Atmospheric Measurement Techniques, 12, 4903–4929, https://doi.org/10.5194/amt-12-4903-2019, 2019.

Gjorgjievska, S. and Raymond, D. J.: Interaction between dynamics and thermodynamics during tropical cyclogenesis, Atmos. Chem. Phys., 14, 3065–3082, https://doi.org/10.5194/acp-14-3065-2014, 2014.

Harnisch, F. and Weissmann, M.: Sensitivity of Typhoon Forecasts to Different Subsets of Targeted Dropsonde Observations, Monthly Weather Review, 138, 2664–2680, 2010.

Harnisch, F., Weissmann, M., Cardinali, C., and Wirth, M.: Experimental assimilation of DIAL water vapour observations in the ECMWF global model, Quarterly Journal of the Royal Meteorological Society, 137, 1532–1546, 2011.

Hersbach, H., Bell, B., Berrisford, P., Hirahara, S., Horányi, A., Muñoz-Sabater, J., Nicolas, J., Peubey, C., Radu, R., Schepers, D., Simmons, A., Soci, C., Abdalla, S., Abellan, X., Balsamo, G., Bechtold, P., Biavati, G., Bidlot, J., Bonavita, M., De Chiara, G., Dahlgren, P., Dee, D., Diamantakis, M., Dragani, R., Flemming, J., Forbes, R., Fuentes, M., Geer, A., Haimberger, L., Healy, S., Hogan, R. J., Hólm, E., Janisková, M., Keeley, S., Laloyaux, P., Lopez, P., Lupu, C., Radnoti, G., de Rosnay, P., Rozum, I., Vamborg, F., Villaume, S., and Thépaut, J.-N.: The ERA5 global reanalysis, Quarterly Journal of the Royal Meteorological Society, 146, 1999–2049, 2020.

Hodges, K. I., Hoskins, B. J., Boyle, J., and Thorncroft, C.: A Comparison of Recent Reanalysis Datasets Using Objective Feature Tracking: Storm Tracks and Tropical Easterly Waves, Monthly Weather Review, 131, 2012–2037, 2003.

Janiga, M. A. and Thorncroft, C. D.: Regional differences in the kinematic and thermodynamic structure of African easterly waves, Quarterly Journal of the Royal Meteorological Society, 139, 1598–1614, 2013.

Keil, C. and Cardinali, C.: The ECMWF reanalysis of the MAP Special Observing Period, Quarterly Journal of the Royal Meteorological Society, 130, 2827–2849, https://doi.org/https://doi.org/10.1256/qj.03.89, 2004.

Kiladis, G. N., Thorncroft, C. D., and Hall, N. M. J.: Three-Dimensional Structure and Dynamics of African Easterly Waves. Part I: Observations, Journal of the Atmospheric Sciences, 63, 2212–2230, 2006.

López Carrillo, C. and Raymond, D. J.: Retrieval of three-dimensional wind fields from Doppler radar data using an efficient two-step approach, Atmospheric Measurement Techniques, 4, 2717–2733, https://doi.org/10.5194/amt-4-2717-2011, 2011.

Mekonnen, A., Thorncroft, C. D., and Aiyyer, A. R.: Analysis of Convection and Its Association with African Easterly Waves, Journal of Climate, 19, 5405–5421, 2006.

Molinari, J. and Vollaro, D.: Planetary- and Synoptic-Scale Influences on Eastern Pacific Tropical Cyclogenesis, Monthly Weather Review, 128, 3296–3307, 2000.

Petersen, W. A., Cifelli, R., Boccippio, D. J., Rutledge, S. A., and Fairall, C.: Convection and Easterly Wave Structures Observed in the Eastern Pacific Warm Pool during EPIC-2001, J. Atmos. Sci., 60, 1754–1773, 2003.

Raymond, D. J. and Fuchs-Stone, Ž.: Emergent Properties of Convection in OTREC and PREDICT, Journal of Geophysical Research: Atmospheres, 126, e2020JD033 585, 2021.

Raymond, D. J. and López Carrillo, C.: The vorticity budget of developing typhoon Nuri (2008), Atmospheric Chemistry and Physics, 11, 147–163, https://doi.org/10.5194/acp-11-147-2011, 2011.

Raymond, D. J. and Sessions, S. L.: Evolution of convection during tropical cyclogenesis, Geophys. Res. Lett., 34, L06 811, https://doi.org/10.1029/2006GL028607, 2007.

Raymond, D. J., Esbensen, S. K., Paulson, C., Gregg, M., Bretherton, C. S., Petersen, W. A., Cifelli, R., Shay, L. K., Ohlmann, C., and Zuidema, P.: EPIC2001 and the coupled ocean-atmosphere system of the tropical east Pacific, Bull. Amer. Meteor. Soc., 85, 1341–1354, 2004.

Raymond, D. J., Gjorgjievska, S., Sessions, S. L., and Fuchs, Ž.: Tropical cyclogenesis and mid-level vorticity, Australian Meteorological and Oceanographic Journal, 64, 11–25, 2014.

Ruti, P. and Dell'Aquila, A.: The twentieth century African easterly waves in reanalysis systems and IPCC simulations, from intra-seasonal to inter-annual variability, Climate Dynamics, 35, 1099–1117, 2010.

Rydbeck, A. V. and Maloney, E. D.: On the Convective Coupling and Moisture Organization of East Pacific Easterly Waves, Journal of the Atmospheric Sciences, 72, 3850–3870, 2015.

Schindler, M., Weissmann, M., Schäfler, A., and Radnoti, G.: The Impact of Dropsonde and Extra Radiosonde Observations during NAWDEX in Autumn 2016, Monthly Weather Review, 148, 809–824, 2020.

Schmit, T. J., Griffith, P., Gunshor, M. M., Daniels, J. M., Goodman, S. J., and Lebair, W. J.: A Closer Look at the ABI on the GOES-R Series, pp. –, 2017.

Sentić, S. and Sessions, S. L.: Idealized modeling of convective organization with changing sea surface temperatures using multiple equilibria in weak temperature gradient simulations, Journal of Advances in Modeling Earth Systems, 9, 1431–1449, 2017.

Sentić, S., Sessions, S. L., and Fuchs, Ž.: Diagnosing DYNAMO convection with weak temperature gradient simulations, Journal of Advances in Modeling Earth Systems, 7, 1849–1871, https://doi.org/10.1002/2015MS000531, 2015.

Serra, Y. L., Kiladis, G. N., and Hodges, K. I.: Tracking and Mean Structure of Easterly Waves over the Intra-Americas Sea, Journal of Climate, 23, 4823–4840, 2010.

Sessions, S. L., Herman, M. J., and Sentić, S.: Convective response to changes in the thermodynamic environment in idealized weak temperature gradient simulations, Journal of Advances in Modeling Earth Systems, 7, 712–738, 2015.
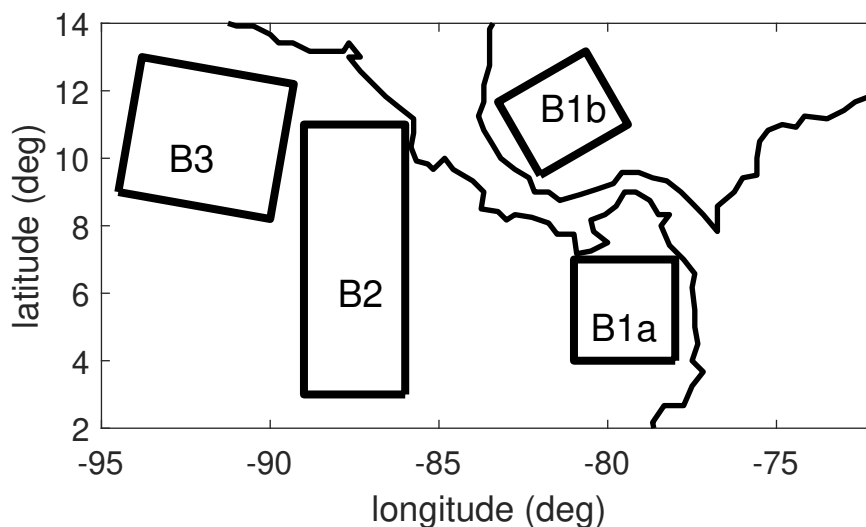
Figure 1. Location of the flight boxes in the OTREC field campaign.

Tompkins, A. M., Diongue-Niang, A., Parker, D. J., and Thorncroft, C. D.: The African easterly jet in the ECMWF
Integrated Forecast System: 4D-Var analysis, Quarterly Journal of the Royal Meteorological Society, 131, 2861–2885,
https://doi.org/https://doi.org/10.1256/qj.04.136, 2005.

UCAR/NCAR Earth Observing Laboratory, Voemel, H.: NCAR/EOL AVAPS Dropsonde QC Data, UCAR/NCAR - Earth Observing Labo-
ratory, pp. –, https://doi.org/doi.org/10.26023/EHRT-TN96-9W04, 2019.

Vömel, H., Goodstein, M., Tudor, L., Witte, J., Fuchs-Stone, Ž., Sentić, S., Raymond, D., Martinez-Claros, J., Juračić, A., Maithel, V.,
and Whitaker, J. W.: High-resolution in situ observations of atmospheric thermodynamics using dropsondes during the Organization of
Tropical East Pacific Convection (OTREC) field campaign, Earth System Science Data, 13, 1107–1117, https://doi.org/10.5194/essd-13-
1107-2021, 2021.

Zehnder, J. A.: The Interaction of Planetary-Scale Tropical Easterly Waves with Topography: A Mechanism for the Initiation of Tropical
Cyclones, Journal of Atmospheric Sciences, 48, 1217–1230, 1991.

Zehnder, J. A., Powell, D. M., and Ropp, D. L.: The Interaction of Easterly Waves, Orography, and the Intertropical Convergence Zone in
the Genesis of Eastern Pacific Tropical Cyclones, Monthly Weather Review, 127, 1566–1585, 1999.
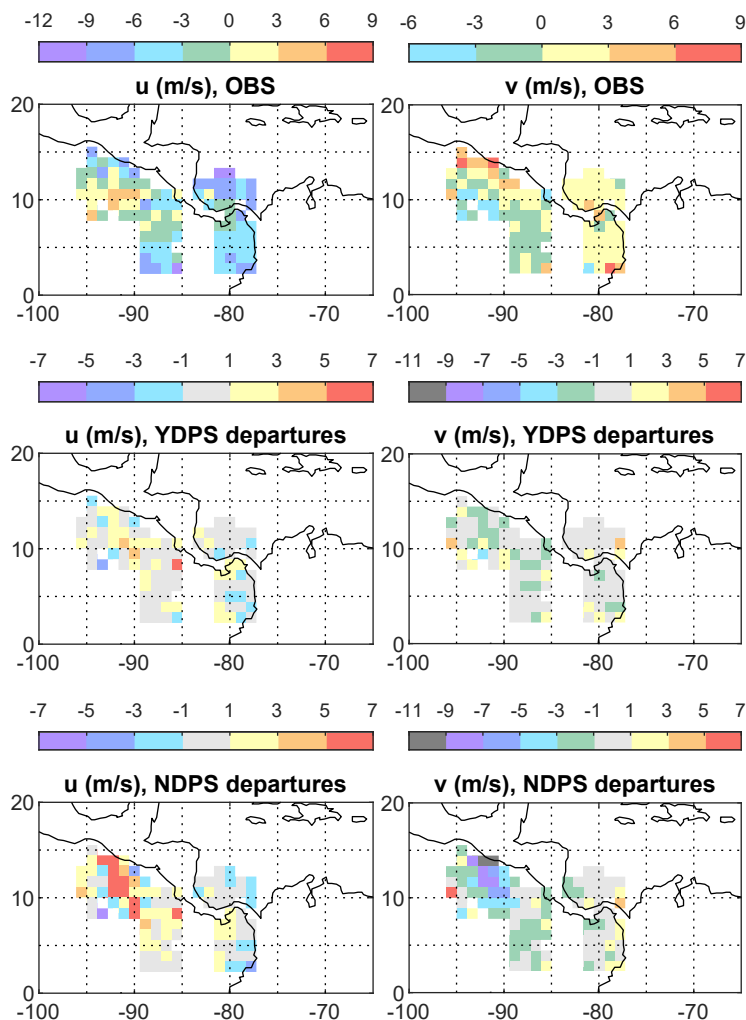
Figure 2. The horizontal distribution of mean departures (defined in equation 1) for zonal (left) and meridional wind (right), at 700 hPa. The top row shows mean dropsonde observations, middle row departures of the control (YDPS) experiment, and bottom row departures of the denial (NDPS) experiment.
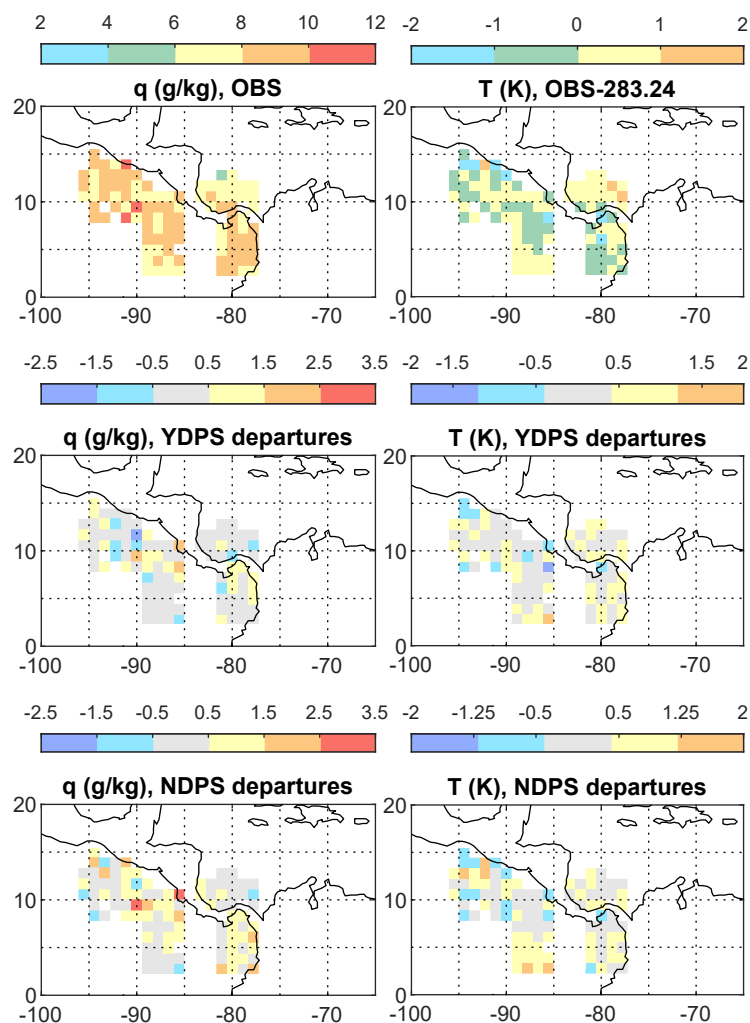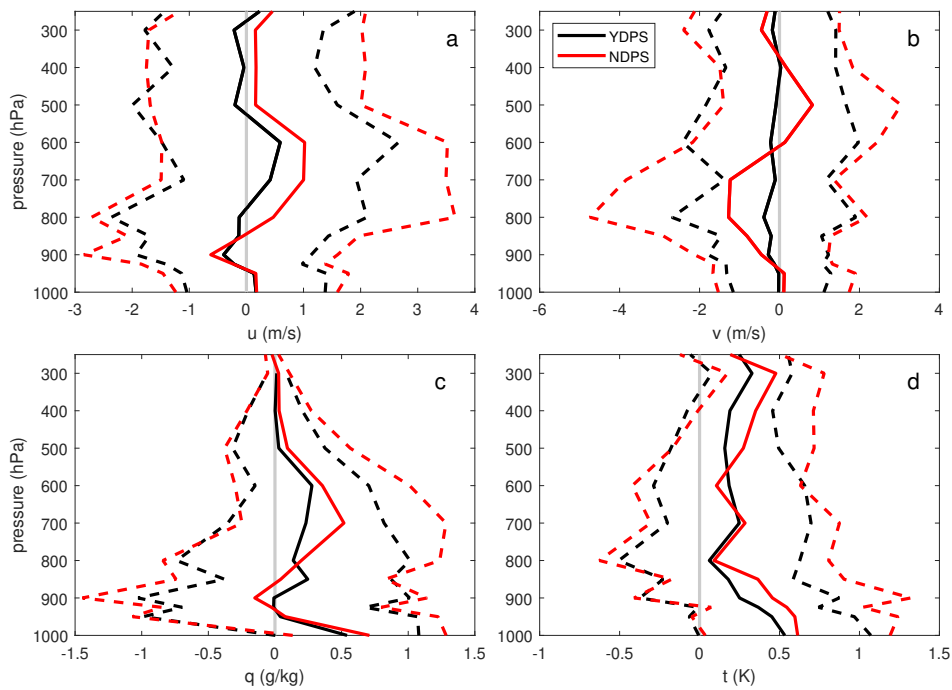
Figure 3. The horizontal distribution of mean departures (defined in equation 1) for mixing ratio (left) and potential temperature (right), at 700 hPa. The top row shows mean dropsonde observations, middle row departures of the control (YDPS) experiment, and bottom row departures of the denial (NDPS) experiment.

Figure 4. The mean (solid line) and one standard deviation (dashed line) of departures from the observations, for a) zonal wind, b) meridional wind, c) mixing ratio, and d) potential temperature, for the control run in black and the dropsonde denial experiment in red.
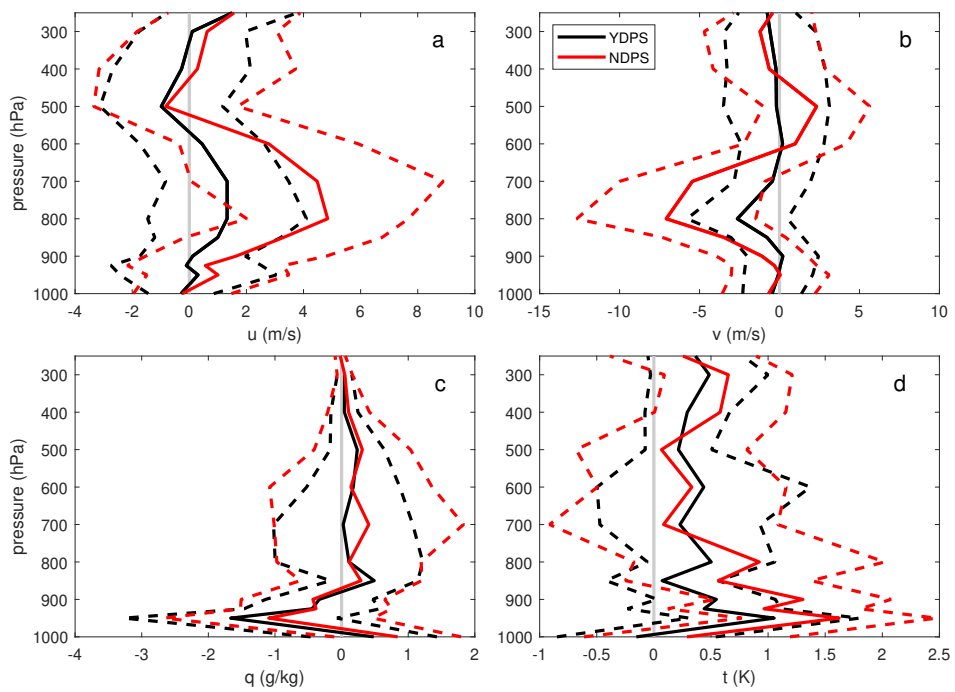
Figure 5. Similar to Figure 4, but for the special case of joint research flight with NOAA P3 on Aug 18.
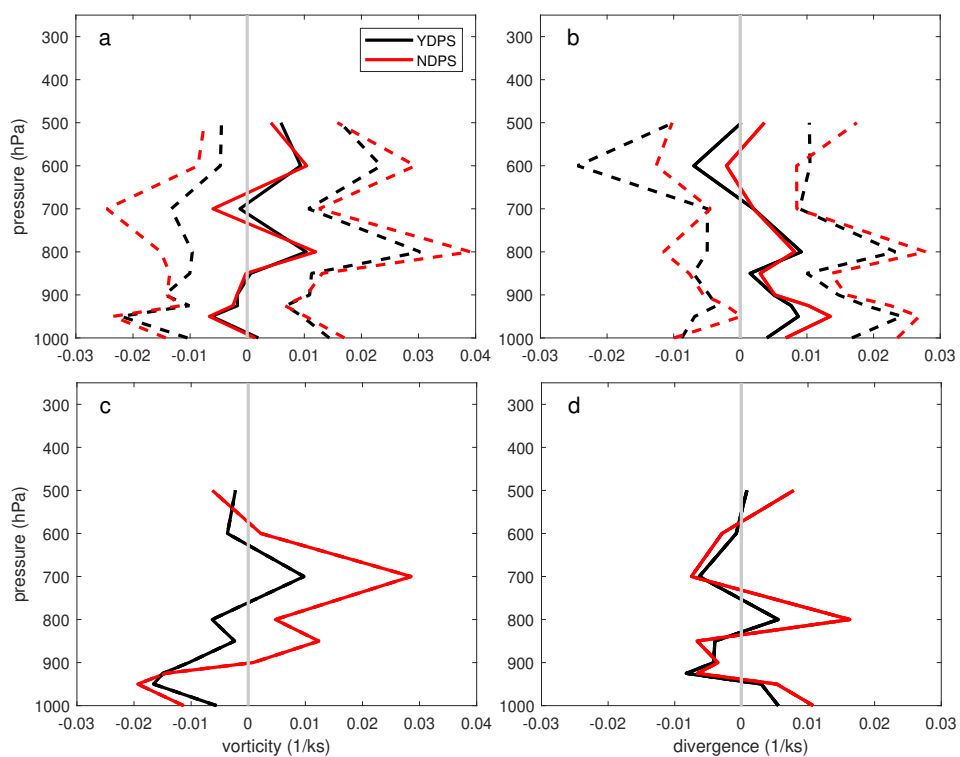
Figure 6. Similar to Figure 4, but for a) vorticity, all cases, b) divergence, all cases, c) vorticity, B3 box case, and d) divergence, B3 box case.
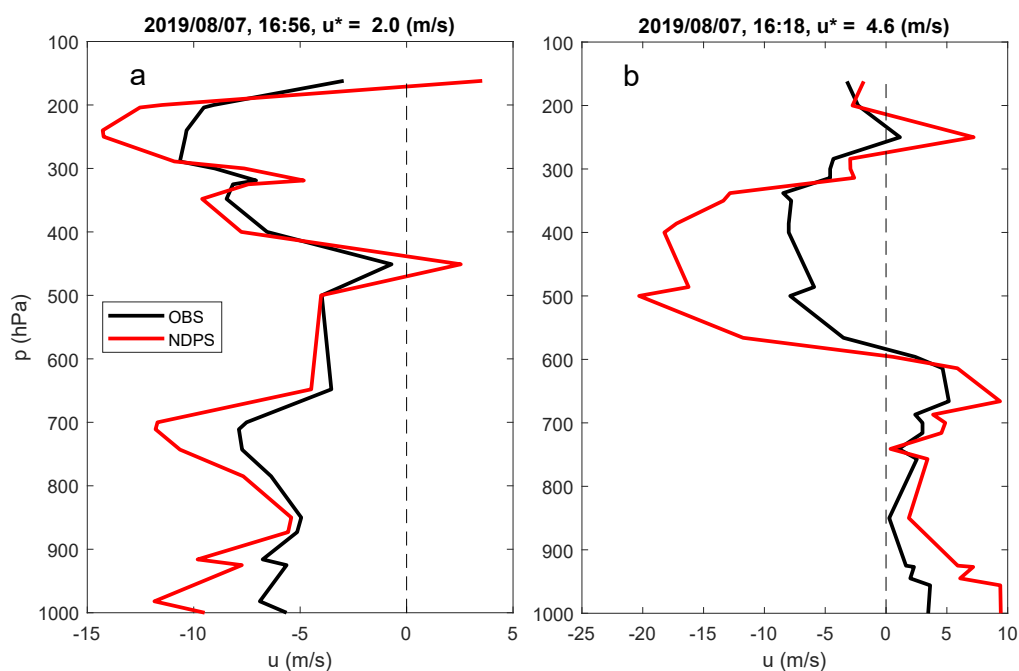
Figure 7. Sample zonal wind observed soundings (black) and their NDPS experiment counter part (red). The value of vertically integrated departures $u*$, which quantify how close the model profile is to the observed, are shown above each plot. Panel a shows a zonal wind profile with a smaller vertically integrated departure compared to to the profile shown in panel b.
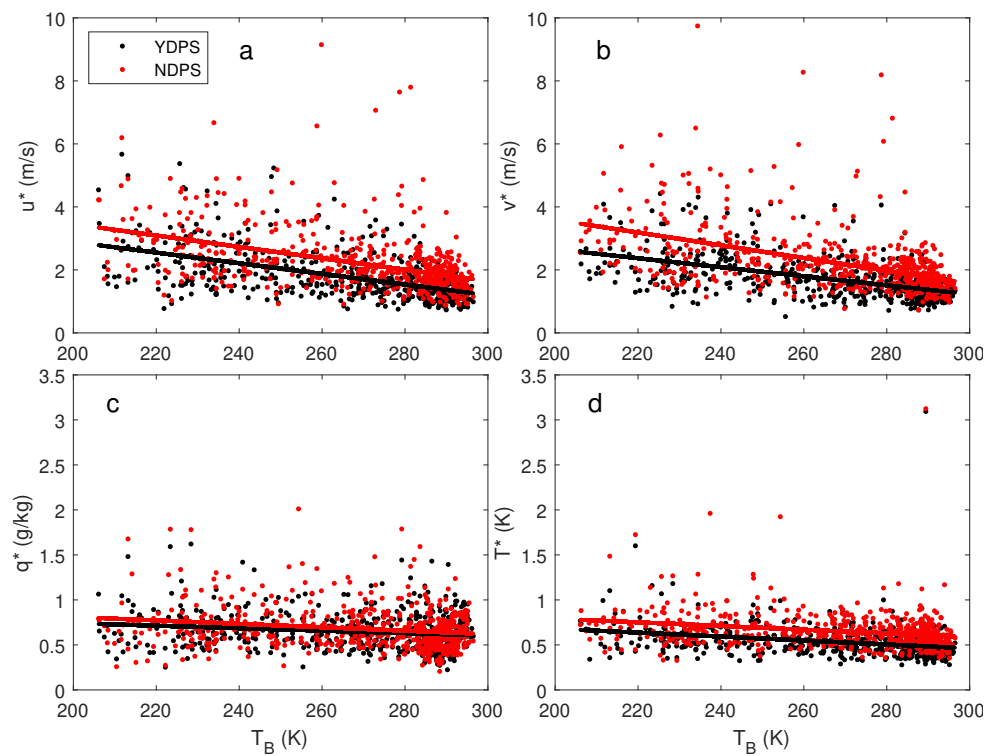
Figure 8. Vertically integrated departure of a) zonal wind, b) meridional wind, c) mixing ratio, and d) potential temperature, versus infrared temperature. See text for discussion.
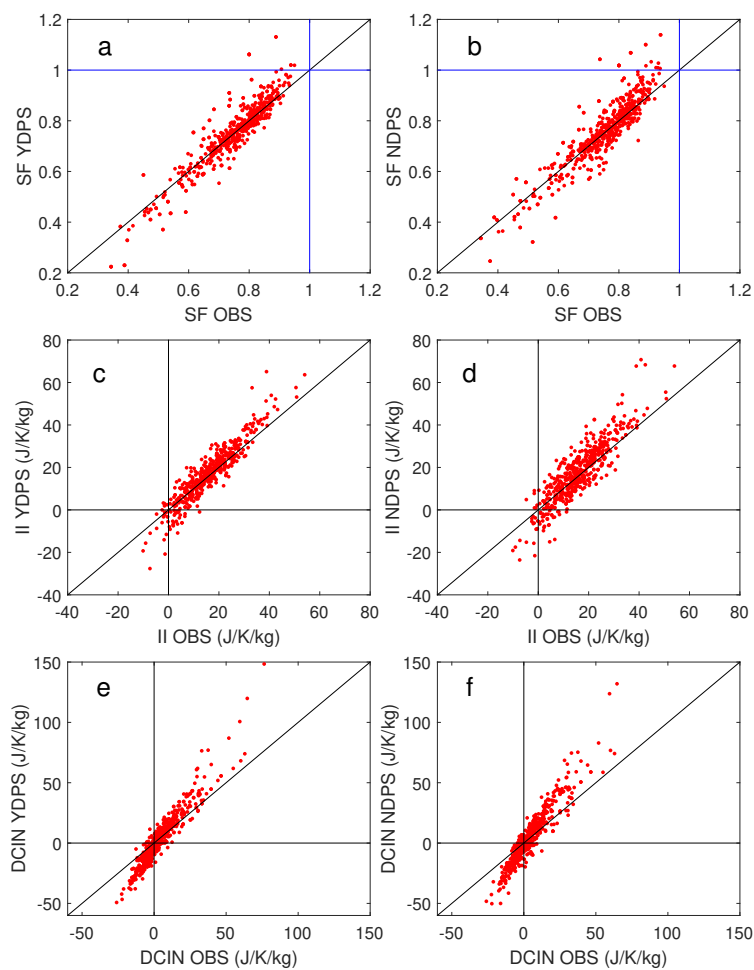
Figure 9. a) saturation fraction, observations vs YDPS, and b) saturation fraction, YDPS vs NDPS, c) Instability index, observations vs YDPS, d) instability index, YDPS vs NDPS, e) DCIN, observations vs YDPS, and f) DCIN, YDPS vs NDPS.
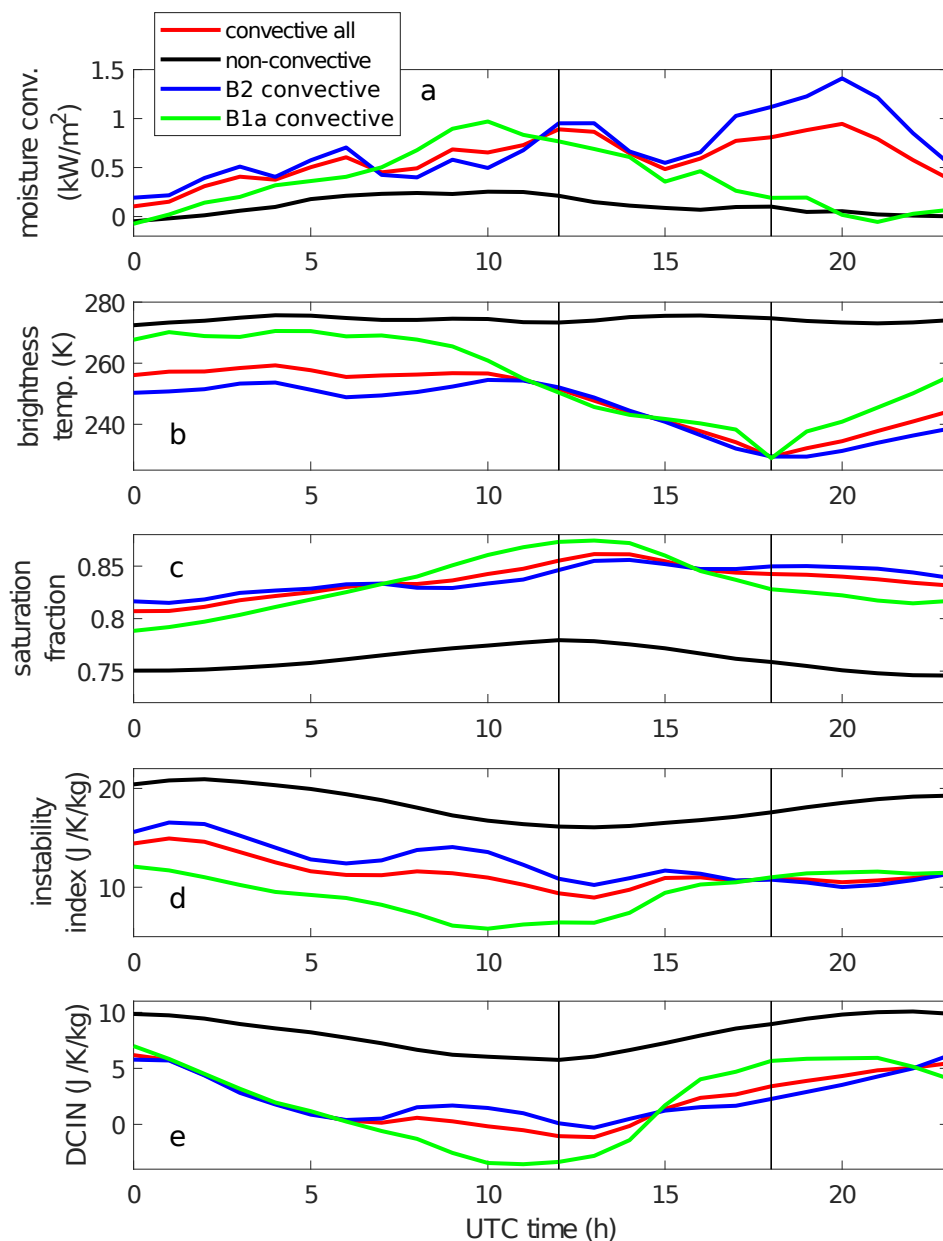
Figure 10. EC model time series composites of: a) moisture convergence, b) infrared temperature (from satellite observations), c) saturation fraction, d) instability index, and e) DCIN. Non-convective time series, defined as having moisture convergence lower than 0.5 kW m^{-2}, are shown in black, while convective time series, defined as having moisture convergence larger than 2.0 kW m^{-2}, are shown in red. Convective time series (red) are also decomposed into the East Pacific box (blue), and the Colombian box (green). Vertical thin black lines indicate the period when the dropsondes were deployed in most research flights.